

# Exact analytical PGSE signal for diffusion confined to a cylindrical surface using a spectral Laplacian formalism

Erick J Canales-Rodríguez<sup>1,2,3,\*</sup>, Chantal M.W. Tax<sup>4,5</sup>, Juan Manuel Górriz<sup>1,2,3</sup>, Derek K. Jones<sup>5</sup>,

Jean-Philippe Thiran<sup>6,7,8</sup>, Jonathan Rafael-Patiño<sup>6,7</sup>

<sup>1</sup> Department of Signal Theory, Networking and Communications, University of Granada, Granada, Spain

<sup>2</sup> Andalusian Research Institute in Data Science and Computational Intelligence (DaSCI), University of Granada, Spain

<sup>3</sup> Research Centre for Information and Communication Technologies (CITIC), University of Granada, Granada, Spain

<sup>4</sup> Image Sciences Institute, University Medical Center Utrecht, The Netherlands.

<sup>5</sup> Cardiff University Brain Research Imaging Centre (CUBRIC), Cardiff University, Cardiff, Wales, United Kingdom.

<sup>6</sup> Signal Processing Laboratory 5 (LTS5), Ecole Polytechnique Fédérale de Lausanne (EPFL), Lausanne, Switzerland.

<sup>7</sup> Computational Medical Imaging & Machine Learning Section, Center for Biomedical Imaging (CIBM), Lausanne, Switzerland

<sup>8</sup> Department of Radiology, Centre Hospitalier Universitaire Vaudois (CHUV), Lausanne, Switzerland

\* Corresponding author: [ejcanalesr@ugr.es](mailto:ejcanalesr@ugr.es)

## Abstract

Pulsed-gradient spin-echo (PGSE) MRI experiments probe molecular self-diffusion through spin phase accumulation under time-dependent magnetic field gradients. For diffusion confined to cylindrical surfaces, existing analytical signal models typically rely on the narrow-pulse limit, approximate treatments of finite gradient durations, or the Gaussian phase approximation, which become increasingly inaccurate at high diffusion weightings. Here, we derive an exact analytical solution of the Bloch–Torrey equation for diffusion confined to a cylindrical surface under finite PGSE gradients and obtain the corresponding diffusion MRI signal expression valid for arbitrary gradient durations and separations. The derivation is based on a spectral matrix formalism of the Laplace operator in the eigenbasis of the confining geometry. The signal is expressed as a product of non-commuting matrix exponentials, without approximations to the diffusion propagator or the spin phase distribution. We further introduce a reduced real spectral basis exploiting the symmetry of the cylindrical surface, substantially improving computational efficiency. Building on this exact formulation, we develop efficient numerical strategies for repeated signal evaluations, including a Strang splitting approximation of the matrix exponentials and an efficient computation of the spherical mean signal using Gauss–Legendre quadrature. The analytical signal is validated against Monte Carlo simulations over a wide range of cylinder radii and experimental parameters. The accelerated implementations are benchmarked against the exact formulation to quantify accuracy–runtime trade-offs. These results establish a computationally efficient framework for evaluating directional and orientationally averaged diffusion MRI signals in applications requiring large numbers of model evaluations.

**Keywords:** Diffusion MRI; Laplace operator; Pulsed-gradient spin-echo sequence; Cylindrical surface; Monte Carlo diffusion simulations; Myelin sheath radius.

## 1. Introduction

Magnetic Resonance Imaging (MRI) experiments sensitized to molecular self-diffusion provide a powerful framework to probe transport processes in confined environments and to infer geometric features of restricting boundaries in porous media and biological tissues<sup>1–4</sup>. In pulsed-gradient spin-echo (PGSE) experiments<sup>5</sup>, diffusion sensitization arises from the accumulation of spin phase under time-dependent magnetic field gradients, such that the measured macroscopic signal reflects ensemble-averaged properties of the underlying stochastic motion. Establishing rigorous links between the measured signal and the geometry of confinement remains a central problem in the theory of diffusion MRI (dMRI)<sup>6–18</sup>.

From a theoretical perspective, the dMRI signal from water molecules in a bounded domain can be described exactly by solving the Bloch–Torrey equation. Spectral and matrix-based approaches employing the eigenfunctions of the Laplace operator have been developed to address this problem<sup>19–28</sup>. These frameworks provide a rigorous description of restricted diffusion and, in principle, allow one to treat arbitrary gradient waveforms and boundary conditions<sup>29,30</sup>. However, for specific geometries of interest, practical signal models often adopt simplifying assumptions (most notably the narrow-pulse limit, approximate treatments of finite gradient durations<sup>31</sup>, or the Gaussian-phase approximation<sup>32–34</sup>) in order to obtain expressions that are analytically tractable and computationally efficient.

Diffusion confined to cylindrical surfaces constitutes a particularly relevant case. In biological tissues, this geometry has been proposed as an effective model for myelin water diffusion, in which water molecules are constrained to move along the surface of the myelin sheath surrounding axons<sup>35,36</sup>. This assumption is supported by the ultrastructure of myelin, where adjacent lamellae are separated by narrow aqueous gaps with an effective thickness of approximately 3–4 nm, as inferred from diffraction- and scattering-based reconstructions<sup>37,38</sup>. In a previous study, we derived an exact analytical expression for the PGSE signal arising from diffusion confined to a cylindrical surface in the narrow-pulse limit and proposed an approximate extension to account for finite gradient durations<sup>35</sup>. While that formulation showed good agreement with Monte Carlo simulations over a broad range of experimental conditions, noticeable discrepancies emerged for large diffusivities and relatively high diffusion weightings, highlighting the limitations of the approximations when finite gradient pulse effects become significant.

The main objective of the present work is to resolve this limitation by deriving an exact analytical solution of the Bloch–Torrey equation for diffusion taking place on the two-dimensional cylindrical manifold, without invoking any approximation on the diffusion propagator, resulting spin phase distribution, or gradient pulse duration. The derivation is based on the spectral matrix formalism of the Laplace operator<sup>29,30</sup>, specifically constructed for the cylindrical surface geometry. By explicitly accounting for the non-commutativity of the operators involved during the different segments of the PGSE sequence, we obtain a closed-form dMRI signal expression valid for arbitrary combinations of rectangular gradient duration and separation.

The paper is organized as follows. Section 2 outlines the theoretical framework for describing confined diffusion in PGSE experiments using the Laplacian spectral matrix formalism. In Section 3, this framework is applied to diffusion confined to a cylindrical surface, and the resulting analytical signal expression is derived. Building on this exact formulation, we also develop efficient numerical strategies for repeated signal evaluations, including a Strang splitting approximation and an efficient computation of the spherical mean signal using Gauss–Legendre quadrature. Details of the Monte Carlo diffusion simulations used for numerical validation are also provided. Section 4 presents the comparison between analytical and Monte

Carlo signals and benchmarks the accelerated implementations against the exact formulation to quantify accuracy–runtime trade-offs. The scope and limitations of the proposed approach are discussed in Section 5. Additional technical details of the mathematical derivations are provided in the Appendices.

## 2 Theory

In this section, we briefly recall the theoretical framework for describing confined diffusion based on the spectral decomposition of the Laplace operator. The use of Laplace operator eigenfunctions to solve the Bloch–Torrey equation was originally introduced by Robertson<sup>19</sup>, and subsequently extended through a variety of analytical and numerical approaches. Notable developments include the multiple narrow-pulse approximation<sup>20</sup>, matrix-based formulations enabling efficient numerical implementations<sup>21,22</sup>, and additional spectral treatments<sup>24,39</sup>. A more complete theoretical description was later formulated by Axelrod and Sen<sup>25</sup> and further generalized and reformulated within the multiple correlation function framework by Grebenkov<sup>28</sup>. In what follows, we summarize the key relations of this spectral matrix approach that are required for the present work, before applying it to diffusion confined to a cylindrical surface.

### 2.1 Bloch–Torrey equation and spectral approach

The Bloch-Torrey equation in the rotating frame of reference, describing the time evolution of the complex-valued transverse magnetization  $M(\mathbf{r}, t)$ , arising from spins diffusing with diffusion coefficient  $D$  in a confined/bounded domain  $\Omega$  is<sup>40</sup>

$$\frac{\partial M(\mathbf{r}, t)}{\partial t} = D \nabla_{\Omega, B}^2 M(\mathbf{r}, t) - i\gamma G(t)(\mathbf{g} \cdot \mathbf{r}) M(\mathbf{r}, t), \quad (1)$$

where  $G(t)$  is the magnitude of the applied time-dependent linear magnetic field gradient pointing along the unit vector  $\mathbf{g}$ ,  $\mathbf{r}$  is the spin’s spatial position vector,  $\gamma$  is the gyromagnetic ratio of the nuclei, and  $\nabla_{\Omega, B}^2$  denotes the Laplace operator  $\nabla^2$  on the domain  $\mathbf{r} \in \Omega$  where the diffusion process takes place, which depends on the boundary conditions describing how the spins interact with the boundaries (e.g.,  $B = \{\text{Neumann, Dirichlet, Robin}\}$ ).

In practice, it is convenient to represent  $M(\mathbf{r}, t)$  in the orthonormal basis of eigenfunctions  $\{\phi_n\}$  resulting from the spectral decomposition of the Laplace operator  $\nabla_{\Omega, B}^2$ . These complex-valued eigenfunctions are determined by the following eigenvalue problem<sup>29</sup>:

$$-\nabla_{\Omega, B}^2 \phi_n(\mathbf{r}) = \lambda_n \phi_n(\mathbf{r}), \quad (2)$$

where depending on the geometry of the problem,  $n$  belongs to the set of natural numbers  $n \in \mathbb{N} = \{0, 1, \dots\}$  or to the set of integers  $n \in \mathbb{Z} = \{-\infty, \dots, -1, 0, 1, \dots, \infty\}$ . The associated eigenvalues are

ordered as  $0 \leq \lambda_0 < \lambda_1 < \dots$  when  $n \in \mathbb{N}$ , or  $\dots > \lambda_{-1} > \lambda_0 < \lambda_1 < \dots$  when  $n \in \mathbb{Z}$ , and the orthonormal eigenfunctions satisfy the property:

$$\int_{\Omega} \phi_n(\mathbf{r}) \phi_m^*(\mathbf{r}) d\mathbf{r} = \delta_{n,m}, \quad (3)$$

where  $\phi_m^*$  is the complex-conjugate of  $\phi_m$  and  $\delta_{nm}$  is the Kronecker delta: it is equal to 1 if  $n = m$ , and 0 if  $n \neq m$ .

In this basis, the magnetization can be expanded as:

$$M(\mathbf{r}, t) = \sum_n c_n(t) \phi_n(\mathbf{r}), \quad (4)$$

where  $c_n(t)$  are time-dependent functions to be estimated.

Substituting Eq. (4) into Eq. (1), and using the definition in Eq. (2), we obtain

$$\sum_n \frac{\partial c_n(t)}{\partial t} \phi_n(\mathbf{r}) = -D \sum_n c_n(t) \lambda_n \phi_n(\mathbf{r}) - i\gamma G(t) (\mathbf{g} \cdot \mathbf{r}) \sum_n c_n(t) \phi_n(\mathbf{r}). \quad (5)$$

This relationship can be simplified by multiplying both sides of the equation by  $\phi_m^*$ , then integrating across the spatial variable and using the identity in Eq (3), which results in

$$\frac{\partial c_n(t)}{\partial t} = -D c_n(t) \lambda_n - i\gamma G(t) \sum_n c_n(t) \int_{\Omega} \phi_n(\mathbf{r}) (\mathbf{g} \cdot \mathbf{r}) \phi_m^*(\mathbf{r}) d\mathbf{r}. \quad (6)$$

By defining a column vector of time-dependent functions, i.e.,  $\mathbf{c}(t) = [c_0(t), c_1(t), \dots]^T$  when  $n \in \mathbb{N}$ , or  $\mathbf{c}(t) = [\dots, c_{-1}(t), c_0(t), c_1(t), \dots]^T$  when  $n \in \mathbb{Z}$ , we obtain the following system of equations in matrix-form:

$$\frac{\partial \mathbf{c}(t)}{\partial t} = -D \mathbf{\Lambda} \mathbf{c}(t) - i\gamma G(t) \mathbf{B} \mathbf{c}(t), \quad (7)$$

where  $\mathbf{\Lambda}$  is a diagonal matrix of the eigenvalues estimated from Eq. (2):  $\mathbf{\Lambda} = \text{diag}([\lambda_0, \lambda_1, \dots])$  when  $n \in \mathbb{N}$ , or  $\mathbf{\Lambda} = \text{diag}([\dots, \lambda_{-1}, \lambda_0, \lambda_1, \dots])$  when  $n \in \mathbb{Z}$ . The entries of matrix  $\mathbf{B}$  are determined by solving the integral

$$B_{nm} = \int_{\Omega} \phi_n(\mathbf{r}) (\mathbf{g} \cdot \mathbf{r}) \phi_m^*(\mathbf{r}) d\mathbf{r}. \quad (8)$$

The solution to the system of differential equations in Eq. (7) is given by <sup>24,39</sup>

$$\mathbf{c}(t) = \Gamma e^{-\int_0^t (D\mathbf{A} + i\gamma G(t)\mathbf{B}) dt} \mathbf{c}(0), \quad (9)$$

where  $\Gamma e$  denotes the time-ordered matrix exponential and  $\mathbf{c}(0)$  is the vector evaluated at time zero. In next sections we will determine matrices  $\mathbf{A}$  and  $\mathbf{B}$  for the confining domain under study, but first, we will relate the dMRI signal with the time dependent vector  $\mathbf{c}(t)$  and the eigenfunctions in the next subsection.

## 2.2 Diffusion MRI signal: Expansion on the spectral basis

The measured dMRI signal is obtained by spatially integrating the transverse magnetization, which can be represented in the basis of eigenfunctions introduced in the previous section:

$$\begin{aligned} E(t) &= \int_{\Omega} M(\mathbf{r}, t) d\mathbf{r} \\ &= \sum_n c_n(t) \int_{\Omega} \phi_n(\mathbf{r}) d\mathbf{r} \\ &= \mathbf{w} \cdot \mathbf{c}(t), \end{aligned} \quad (10)$$

where  $\mathbf{w}$  is the vector with entries equal to the spatial integral of the eigenfunctions:

$$\mathbf{w} = \left[ \int_{\Omega} \phi_0(\mathbf{r}) d\mathbf{r}, \int_{\Omega} \phi_1(\mathbf{r}) d\mathbf{r}, \dots \right] \text{ when } n \in \mathbb{N}, \text{ or } \mathbf{w} = \left[ \dots, \int_{\Omega} \phi_{-1}(\mathbf{r}) d\mathbf{r}, \int_{\Omega} \phi_0(\mathbf{r}) d\mathbf{r}, \int_{\Omega} \phi_1(\mathbf{r}) d\mathbf{r}, \dots \right]$$

when  $n \in \mathbb{Z}$ . This expression establishes a direct relationship between the dMRI signal and vector  $\mathbf{c}(t)$ .

## 2.3 Analytical solution for the PGSE experiment

In a PGSE sequence with two rectangular pulses of duration  $\delta$ , separated by  $\Delta - \delta$ , the gradient function can be represented as piecewise constant in 3 segments<sup>5</sup>:

1. First pulse:  $G(t) = G$  for  $t \in [0, \delta]$ ,
2. Free evolution:  $G(t) = 0$  for  $t \in (\delta, \Delta]$ ,
3. Second pulse:  $G(t) = -G$  for  $t \in (\Delta, \Delta + \delta]$ .

For this sequence, the general solution given in Eq. (9) becomes<sup>24,29,39</sup>

$$\begin{aligned} \mathbf{c}(t) &= e^{-\int_{\Delta}^{\Delta+\delta} (D\mathbf{A} + i\gamma G(t)\mathbf{B}) dt} e^{-\int_{\delta}^{\Delta} (D\mathbf{A}) dt} e^{-\int_0^{\delta} (D\mathbf{A} + i\gamma G(t)\mathbf{B}) dt} \mathbf{c}(0), \\ &= e^{-(D\mathbf{A} - i\gamma G\mathbf{B})\delta} e^{-D(\Delta - \delta)\mathbf{A}} e^{-(D\mathbf{A} + i\gamma G\mathbf{B})\delta} \mathbf{c}(0). \end{aligned} \quad (11)$$

It should be noted that this relationship involves matrix exponentials applied to square matrices, which are not equal to the ordinary exponential function. As the involved matrices do not commute, we cannot regroup them into a single exponential. The numerical evaluation must be performed by multiplying the

exponential matrices from right to left: propagating the effect of the first gradient pulse on the initial state, then including the effect of the free evolution part on the resulting vector, and finally the effect of the second pulse. Nevertheless, as matrix  $\Lambda$  is diagonal, the matrix exponential in the second term in Eq. (11) can be efficiently computed by exponentiating each entry on the main diagonal.

### 3. Methods

#### 3.1 Diffusion confined on cylindrical surfaces: Computing matrices $\Lambda$ and $\mathbf{B}$

After having reviewed the general theory of the spectral approach and resulting dMRI signal, the last missing ingredient of the recipe is to compute the matrices  $\Lambda$  and  $\mathbf{B}$  for our problem of interest: for diffusion confined to a cylindrical surface.

In this section, we will focus on deriving an expression for the dMRI signal  $E_{\perp}$  for a diffusion gradient applied perpendicularly to the cylinder's main axis, which thus, depends on the spin's displacements on the 2D circumference of the circle perpendicular to this axis.

In polar coordinates, the Laplace operator for this geometry reduces to its angular component part:

$$\nabla_{\Omega, \mathbf{B}}^2 = \frac{1}{r^2} \frac{\partial^2}{\partial \theta^2}, \quad (12)$$

where  $\theta$  is the azimuthal angle and  $r$  is the cylinder/circle radius.

The normalized eigenfunctions of  $\nabla_{\Omega, \mathbf{B}}^2$  are <sup>41</sup>

$$\phi_n = \frac{1}{\sqrt{2\pi}} e^{in\theta}, \quad n \in \mathbb{Z} = \{-\infty, \dots, -1, 0, 1, \dots, \infty\}. \quad (13)$$

By plugging Eq. (13) into Eq. (12) we obtain

$$-\nabla_{\Omega, \mathbf{B}}^2 \phi_n = \frac{1}{r^2} \frac{\partial^2 \phi_n}{\partial \theta^2} = \frac{n^2}{r^2} \frac{1}{\sqrt{2\pi}} e^{in\theta} = \frac{n^2}{r^2} \phi_n. \quad (14)$$

Thus, the eigenvalues are given by (see Eq. (2))  $\lambda_n = \frac{n^2}{r^2}$ , which are used to build matrix  $\Lambda$ :

$$\Lambda = \frac{1}{r^2} \Theta, \quad (15)$$

$$\Theta = \text{diag}([\dots, n^2, \dots, 1, 0, 1, \dots, n^2, \dots]).$$

Note that the eigenvalues are symmetric around the ground mode,  $n = 0$ , and that the 'spatial/angular' integrals of these eigenfunctions are zero, except for the ground mode:

$$\begin{aligned}
\int_0^{2\pi} \phi_n(\theta) d\theta &= \frac{1}{\sqrt{2\pi}} \int_0^{2\pi} e^{in\theta} d\theta \\
&= \frac{1}{\sqrt{2\pi}} \left( \int_0^{2\pi} \cos(n\theta) d\theta + i \int_0^{2\pi} \sin(n\theta) d\theta \right) \\
&= \begin{cases} \sqrt{2\pi}, & n = 0, \\ 0, & n \neq 0. \end{cases}
\end{aligned} \tag{16}$$

For this geometry, the elements of matrix  $B_{nm}$  (see Eq. (8); all the details are presented in Appendix A) are:

$$\begin{aligned}
B_{nm} &= \left( \frac{1}{2\pi} \right) r \int_0^{2\pi} \cos(\theta) e^{in\theta} e^{-im\theta} d\theta, \\
&= \frac{r}{2} (\delta_{n,m-1} + \delta_{n,m+1}).
\end{aligned} \tag{17}$$

This matrix can be rewritten as

$$\mathbf{B} = \frac{r}{2} \mathbf{K}, \tag{18}$$

where  $\mathbf{K}$  is a tri-diagonal matrix with 1 on the off-diagonals,  $K_{n,n-1} = K_{n,n+1} = 1$ , and 0 on the main diagonal,  $K_{n,n} = 0$ :

$$\mathbf{K} = \begin{bmatrix} 0 & 1 & & & \\ 1 & 0 & 1 & & \\ & 1 & \ddots & \ddots & \\ & & \ddots & \ddots & 1 \\ & & & 1 & 0 \end{bmatrix}. \tag{19}$$

### 3.2 Optimizing for dimensionality and speed: Recomputing $\mathbf{\Lambda}$ and $\mathbf{B}$

In the previous section we derived the expressions for  $\mathbf{\Lambda}$  and  $\mathbf{B}$  for the basis of eigenfunctions. In practice, it is necessary to truncate the basis up to a maximum order  $n = M$ , resulting in matrices with dimensions of  $(2M + 1) \times (2M + 1)$ , including the ground eigenmode. Since evaluating the matrix exponential terms in Eq. (11) is computationally demanding when  $M$  is large, a more practical alternative is to build a new compact basis (i.e.,  $n \in \mathbb{N}$ ) with the same number of eigenfunctions  $n = M$ , but based on matrices with dimensions of  $(M + 1) \times (M + 1)$ . This reduction is particularly advantageous from a computational point of view. Modern algorithms for evaluating the matrix exponential, as implemented in *MATLAB* and *SciPy*, rely on a scaling-and-squaring strategy combined with Padé rational approximations and are dominated by dense matrix–matrix products, whose computational cost scales cubically with the matrix dimension<sup>42,43</sup>. Therefore, the proposed reduction leads to an expected computational gain

proportional to  $((2M + 1)/(M + 1))^3$ . This corresponds to an ideal speed-up factor of eight in the asymptotic regime of very large  $M$ .

The following construction exploits the symmetry of the eigenfunctions and the fact that the measured signal is real. By adding the eigenfunctions with the same order  $n$  and opposite signs, we get the new functions

$$\begin{aligned}\tilde{\phi}_n &= \frac{1}{\sqrt{2}}(\phi_n + \phi_{-n}) \\ &= \frac{1}{2}\sqrt{\frac{1}{\pi}}e^{in\theta} + \frac{1}{2}\sqrt{\frac{1}{\pi}}e^{-in\theta} \\ &= \sqrt{\frac{1}{\pi}}\cos(n\theta).\end{aligned}\tag{20}$$

Therefore, the new basis to represent the magnetization, as in Eq. (4), is defined as

$$\tilde{\phi}_n = \begin{cases} \frac{1}{\sqrt{2\pi}}, & n=0, \\ \sqrt{\frac{1}{\pi}}\cos(n\theta), & n \geq 1. \end{cases}\tag{21}$$

The normalization factor  $1/\sqrt{2}$  added in Eq. (20) was chosen on purpose, to get an orthonormal basis similar to Eq. (3) satisfying:

$$\int_0^{2\pi} \tilde{\phi}_n(\theta)\tilde{\phi}_m(\theta)d\theta = \delta_{n,m}.\tag{22}$$

This is true in virtue of the following property:

$$\int_0^{2\pi} \cos(n\theta)\cos(m\theta)d\theta = \begin{cases} 2\pi, & n = m = 0, \\ \pi, & n = m \neq 0, \\ 0, & n \neq m. \end{cases}\tag{23}$$

According to this operation, it is possible to transform the  $2M + 1$  vector  $\mathbf{c}(t)$  from the original basis to the compact basis  $\tilde{\mathbf{c}}$  with  $M + 1$  terms as:

$$\mathbf{c} = \mathbf{T}\tilde{\mathbf{c}},\tag{24}$$

where the  $(2M + 1) \times (M + 1)$  transformation matrix is:

$$\mathbf{T} = \begin{bmatrix} 0 & 0 & 0 & 1/\sqrt{2} \\ \vdots & \vdots & \ddots & \vdots \\ 0 & 1/\sqrt{2} & \cdots & 0 \\ 1 & 0 & \cdots & 0 \\ 0 & 1/\sqrt{2} & \cdots & 0 \\ \vdots & \vdots & \ddots & \vdots \\ 0 & 0 & 0 & 1/\sqrt{2} \end{bmatrix}. \quad (25)$$

By using this transformation, we rewrite Eq. (11) in terms of the vector  $\tilde{\mathbf{c}}$  as

$$\tilde{\mathbf{c}}(t) = \mathbf{T}^T e^{-(D\Lambda - i\gamma G\mathbf{B})\delta} e^{-D(\Lambda - \delta)\Lambda} e^{-(D\Lambda + i\gamma G\mathbf{B})\delta} \mathbf{T}\tilde{\mathbf{c}}(0). \quad (26)$$

Notably, in Appendix B, we prove (due to the structure of  $\mathbf{T}$  and the symmetry of matrices  $\Lambda$  and  $\mathbf{B}$ ) the following property:

$$\mathbf{T}^T e^{-\Lambda_3} e^{-\Lambda_2} e^{-\Lambda_1} \mathbf{T} = e^{-\mathbf{T}^T \Lambda_3 \mathbf{T}} e^{-\mathbf{T}^T \Lambda_2 \mathbf{T}} e^{-\mathbf{T}^T \Lambda_1 \mathbf{T}}. \quad (27)$$

Therefore, Eq. (26) can be rewritten as:

$$\tilde{\mathbf{c}}(t) = e^{-(D\tilde{\Lambda} - i\gamma G\tilde{\mathbf{B}})\delta} e^{-D(\Lambda - \delta)\tilde{\Lambda}} e^{-(D\tilde{\Lambda} + i\gamma G\tilde{\mathbf{B}})\delta} \tilde{\mathbf{c}}(0), \quad (28)$$

where

$$\begin{aligned} \tilde{\Lambda} &= \mathbf{T}^T \Lambda \mathbf{T}, \\ &= \text{diag}([\lambda_0, \lambda_1, \dots]), \\ &= \frac{1}{r^2} \tilde{\Theta}, \text{ where } \tilde{\Theta} = \text{diag}([0, 1, \dots, n^2, \dots]), \end{aligned} \quad (29)$$

and

$$\begin{aligned} \tilde{\mathbf{B}} &= \mathbf{T}^T \mathbf{B} \mathbf{T}, \\ &= \frac{r}{2} \tilde{\mathbf{K}}, \text{ where} \\ \tilde{\mathbf{K}} &= \begin{bmatrix} 0 & \sqrt{2} & & & \\ \sqrt{2} & 0 & 1 & & \\ & 1 & \ddots & \ddots & \\ & & \ddots & \ddots & 1 \\ & & & 1 & 0 \end{bmatrix} \end{aligned} \quad (30)$$

The main benefit of working with the compact basis, Eqs. (28)-(30), is that now the matrix exponentials are evaluated on matrices with reduced dimensionality, i.e.,  $(M+1) \times (M+1)$  instead of  $(2M+1) \times (2M+1)$  in the original basis, allowing for a more efficient implementation.

### 3.3 Diffusion confined on cylindrical surfaces: Computing $\mathbf{w}$ and $\mathbf{c}(0)$

According to our previous results, the dMRI signal  $E_{\perp}$  is given by (see Eqs. (10), (28)-(30))

$$E_{\perp}(G, \Delta, \delta) = \mathbf{w} \cdot \left[ e^{-\left(\frac{D}{r^2} \tilde{\Theta} - i \frac{\gamma Gr}{2} \tilde{\mathbf{K}}\right) \delta} e^{-\frac{D(\Delta-\delta)}{r^2} \tilde{\Theta}} e^{-\left(\frac{D}{r^2} \tilde{\Theta} + i \frac{\gamma Gr}{2} \tilde{\mathbf{K}}\right) \delta} \tilde{\mathbf{c}}(0) \right], \quad (31)$$

where  $\tilde{\Theta}$  and  $\tilde{\mathbf{K}}$  are defined in Eqs. (29) and (30).

However, to evaluate this expression we still need to determine  $\mathbf{w}$  from the eigenfunctions (Eq. (21)), and  $\mathbf{c}(0)$  from the initial conditions.

From Eq. (16) we see that the spatial integrals in the diffusion geometry (on the circle's circumference) are zero  $w_n = 0$ , except for the element corresponding to  $n = 0$ :  $\mathbf{w} = [w_0, 0, \dots]$ . This happens because when the ground eigenfunction  $\tilde{\phi}_0(\mathbf{r})$  is constant/spatially uniform, like in our problem, the spatial integrals of all the other eigenfunctions are zero due to the orthogonality property, see Eq. (22).

On the other hand, vector  $\mathbf{c}(0)$  can be determined from the initial conditions, that is, from the value of  $M(\mathbf{r}, t = 0)$ . Assuming a spatially uniform initial magnetization on the cylinder surface implies  $c_n(0) = 0$  for all  $n \neq 0$ , i.e.,  $\mathbf{c}(0) = [1, 0, \dots]^T$ . This follows from the expansion in Eq. (4) for  $t = 0$ , together with the observation that the only spatially constant eigenfunction is the ground state  $\tilde{\phi}_0(\mathbf{r})$ .

Thus, Eq. (31) becomes

$$E_{\perp}(G, \Delta, \delta) = w_0 \cdot \left[ e^{-\left(\frac{D}{r^2} \tilde{\Theta} - i \frac{\gamma Gr}{2} \tilde{\mathbf{K}}\right) \delta} e^{-\frac{D(\Delta-\delta)}{r^2} \tilde{\Theta}} e^{-\left(\frac{D}{r^2} \tilde{\Theta} + i \frac{\gamma Gr}{2} \tilde{\mathbf{K}}\right) \delta} \right]_{0,0}, \quad (32)$$

where we symbolically evaluated the vector multiplications. The subscript in the previous equation indicates that after computing the product of the three matrix exponentials we only take the entry at index  $(0,0)$ , i.e., the first matrix element corresponding to ground mode, the index-term  $n = 0$ .

Note that if we repeat the PGSE experiment for  $G = 0$ , the above expression is simplified to

$$\begin{aligned}
E_{\perp}(G=0, \Delta, \delta) &= w_0 \left[ e^{-\frac{D(\Delta+\delta)}{r^2} \tilde{\Theta}} \right]_{0,0}, \\
&= w_0 e^{-\frac{D(\Delta+\delta)}{r^2} \tilde{\Theta}_{0,0}}, \\
&= w_0,
\end{aligned} \tag{33}$$

where the matrix-exponential becomes the ordinary exponential of the resulting diagonal matrix, and the first element of  $\tilde{\Theta}_{0,0} = 0$ . This happens because in problems where  $\tilde{\phi}_0(\mathbf{r})$  is a constant, like in our case,  $\lambda_0 = 0$  is the only eigenvalue that fulfills the equality given in Eq. (2),  $\nabla_{\Omega, B}^2 \tilde{\phi}_0(\mathbf{r}) = 0 = \lambda_0 \tilde{\phi}_0$ .

Thus, Eq. (32) can be written in the more common normalized form:

$$\frac{E_{\perp}(q, \Delta, \delta)}{E_{\perp}(q=0)} = \left[ e^{-\frac{D\delta}{r^2} \tilde{\Theta} + i \frac{qr}{2} \tilde{\mathbf{K}}} e^{-\frac{D(\Delta-\delta)}{r^2} \tilde{\Theta}} e^{-\frac{D\delta}{r^2} \tilde{\Theta} - i \frac{qr}{2} \tilde{\mathbf{K}}} \right]_{0,0} \tag{34}$$

which is dimensionless and the normalized signal lies in the unit interval [0,1]. Note that we introduced the magnitude of the q-vector as  $q = |\mathbf{q}| = \gamma G \delta$ .

This relationship provides an exact analytical expression for the dMRI signal arising from diffusing spins in a cylindrical surface, when the gradient is applied perpendicularly to the cylinder's axis. Notably, it is not based on any simplifying assumptions about the diffusion propagator, the duration of the gradient pulses, or the distribution of phases. The only approximation involved is numerical, resulting from truncating the number of eigenfunctions and eigenvalues employed to practically evaluate the expression (i.e., the dimensionality of matrices  $\tilde{\Theta}$  and  $\tilde{\mathbf{K}}$ ). Nevertheless, in practice, it usually converges with a few terms as the eigenvalues grow as  $n^2$ .

### 3.4 Exact reduction to a single matrix exponential via conjugation symmetry

A direct evaluation of Eq. (34) requires two matrix exponentials per signal sample (e.g., gradient direction or  $b$ -value). An additional reduction in computational cost follows from noting that the first and third matrix exponentials in Eq. (34) (corresponding to the time intervals in which the diffusion gradients are applied in the PGSE experiment) are complex conjugates of each other. Therefore, in practice, it is sufficient to evaluate only one matrix exponential, while the second one can be obtained by complex conjugation. This strategy reduces the signal evaluation computational cost by approximately a factor of two.

### 3.5 Decoupled diffusive motions and dMRI signal components

In the previous section we derived the analytical dMRI signal expression (Eq. (34)) for the case when the diffusion-encoding gradient is applied perpendicularly to the main cylinder's axis. For an arbitrary gradient orientation, this expression is still valid but some modifications must be implemented.

For an infinitely long cylinder, the diffusion process of spin particles parallel and perpendicular to the cylinder's main axis is statistically independent. As a result, the dMRI signal can be expressed as the product of the signals arising from displacements parallel and perpendicular to the cylinder's axis <sup>44</sup>:

$$E(\mathbf{q}, \Delta, \delta) = E_{\perp}(\mathbf{q}_{\perp}, \Delta, \delta) E_{\parallel}(\mathbf{q}_{\parallel}, \Delta, \delta), \quad (35)$$

where  $\mathbf{q}_{\parallel}$  and  $\mathbf{q}_{\perp}$  are the projection of the q-space vector  $\mathbf{q} = q\hat{\mathbf{g}}$  along the directions parallel and perpendicular to the cylinder's axis,  $\mathbf{q} = \mathbf{q}_{\parallel} + \mathbf{q}_{\perp}$ ; thus their magnitudes are given by  $q_{\parallel} = |\mathbf{q}_{\parallel}| = q \cos(\beta)$  and  $q_{\perp} = |\mathbf{q}_{\perp}| = q \sin(\beta)$ , where  $\beta$  is the angle between the diffusion gradient orientation unit vector  $\hat{\mathbf{g}}$  and the unit vector along the main cylinder's  $\hat{\mathbf{v}}$ . A general detailed derivation of this type of decoupled signal model is provided in <sup>44</sup>.

Since the motion of particles along the cylinder's main axis is unrestricted, we assume 1D Gaussian diffusion with a characteristic myelin water diffusivity  $D$  on the cylinder's surface. The normalized dMRI PGSE signal  $E_{\parallel}(\mathbf{q}_{\parallel}, \Delta, \delta)$  arising from these Gaussian displacements is

$$\frac{E_{\parallel}(\mathbf{q}_{\parallel}, \Delta, \delta)}{E_{\parallel}(\mathbf{q}_{\parallel} = 0)} = e^{-q^2(\Delta - \delta/3)D \cos(\beta)^2}, \quad (36)$$

where  $b = q^2(\Delta - \delta/3)$  is the  $b$ -value.

On the other hand, in the expression for  $E_{\perp}(\mathbf{q}_{\perp}, \Delta, \delta)$  given by Eq. (34) we must replace  $q$  by its projection  $q_{\perp}$  along the plane perpendicular to the cylinder axis. Therefore, the final signal expression in Eq. (35) for an arbitrary gradient orientation becomes

$$\frac{E(q, \hat{\mathbf{g}}, \Delta, \delta)}{E(q=0)} = e^{-q^2(\Delta - \delta/3)D(\hat{\mathbf{g}} \cdot \hat{\mathbf{v}})^2} \left[ e^{-\frac{D\delta}{r^2} \tilde{\Theta} + i \frac{qr\sqrt{1 - (\hat{\mathbf{g}} \cdot \hat{\mathbf{v}})^2}}{2} \tilde{\mathbf{K}}} e^{-\frac{D(\Delta - \delta)}{r^2} \tilde{\Theta}} e^{-\frac{D\delta}{r^2} \tilde{\Theta} - i \frac{qr\sqrt{1 - (\hat{\mathbf{g}} \cdot \hat{\mathbf{v}})^2}}{2} \tilde{\mathbf{K}}} \right]_{0,0}, \quad (37)$$

where we substituted the following trigonometric relationships,  $\cos(\beta)^2 = (\hat{\mathbf{g}} \cdot \hat{\mathbf{v}})^2$  and  $\sin(\beta) = \sqrt{1 - (\hat{\mathbf{g}} \cdot \hat{\mathbf{v}})^2}$ , and made the signal to explicitly depend on the experimental (arguments) parameters of the PGSE sequence.

### 3.6 Strang splitting with $p$ substeps

While in the previous sections we introduced theoretical developments and implementation aspects to accelerate the evaluation of the radial signal component, additional speed-ups are desirable. This is relevant, for example, when a large number of signals must be evaluated repeatedly across diffusion gradient orientations, or across different radii when the signal model is used within a nonlinear fitting procedure (e.g., to estimate the radius from measured data as an inverse problem).

In this section, we employ the second-order Strang splitting (or Strang–Marchuk operator splitting) method<sup>45,46</sup> to obtain an approximate signal, which can significantly accelerate the signal evaluation while providing explicit control of the approximation accuracy. This approach is widely used in different fields, including the simulation of Hamiltonian systems, quantum mechanics (for approximating the time evolution governed by the time-dependent Schrödinger equation), as well as in fluid dynamics and numerical solutions of partial differential equations.

The idea behind this method is to approximate the matrix exponentials in Eq. (37) as

$$e^{-\frac{D\delta}{r^2}\tilde{\Theta}\pm i\frac{qr\sqrt{1-(\hat{\mathbf{g}}\cdot\hat{\mathbf{v}})^2}}{2}\tilde{\mathbf{K}}} \approx \left( e^{-\frac{D\delta}{2pr^2}\tilde{\Theta}} e^{\pm i\frac{qr\sqrt{1-(\hat{\mathbf{g}}\cdot\hat{\mathbf{v}})^2}}{2p}\tilde{\mathbf{K}}} e^{-\frac{D\delta}{2pr^2}\tilde{\Theta}} \right)^p + O\left(\left(\delta/p\right)^2\right), \quad (38)$$

where the approximation error  $O\left(\left(\delta/p\right)^2\right)$  decreases quadratically with the number of substeps  $p$  used to discretize the time interval  $\delta$ . Therefore, the error can be made arbitrarily small by choosing a sufficiently large value of  $p$ .

In our application, the computational gain arises from the fact that the matrices  $\tilde{\Theta}$  and  $\tilde{\mathbf{K}}$ , which are fixed and do not depend on the radius or the sequence parameters (e.g., gradient orientation and gradient strength), now appear inside short-time matrix exponential terms. This allows us to diagonalize  $\tilde{\mathbf{K}}$  (i.e.,  $\tilde{\mathbf{K}} = \mathbf{Q}\mathbf{\Omega}\mathbf{Q}^T$ , where  $\mathbf{\Omega} = \text{diag}(\lambda_0, \dots, \lambda_M)$  and  $\mathbf{Q}^T\mathbf{Q} = \mathbf{I}$ ) and write

$$e^{\pm i\frac{qr\sqrt{1-(\hat{\mathbf{g}}\cdot\hat{\mathbf{v}})^2}}{2p}\tilde{\mathbf{K}}} = \mathbf{Q}e^{\pm i\frac{qr\sqrt{1-(\hat{\mathbf{g}}\cdot\hat{\mathbf{v}})^2}}{2p}\mathbf{\Omega}}\mathbf{Q}^T. \quad (39)$$

Notably, this removes the need to evaluate a dense matrix exponential; the exponential in the second term of the previous equation is applied to a diagonal matrix and can be computed by simply taking the scalar exponential of each diagonal entry. Moreover, the diagonalization of  $\tilde{\mathbf{K}}$  can be precomputed before the signal evaluation.

By substituting Eq. (39) into Eq. (38), we obtain

$$e^{-\frac{D\delta}{r^2}\tilde{\Theta}\pm i\frac{qr\sqrt{1-(\hat{\mathbf{g}}\cdot\hat{\mathbf{v}})^2}}{2}\tilde{\mathbf{K}}} \approx e^{-\frac{D\delta}{2pr^2}\tilde{\Theta}} \mathbf{Q}e^{\pm i\frac{qr\sqrt{1-(\hat{\mathbf{g}}\cdot\hat{\mathbf{v}})^2}}{2p}\mathbf{\Omega}}\mathbf{Q}^T \left( \prod_{i=1}^{p-1} e^{-\frac{D\delta}{pr^2}\tilde{\Theta}} \mathbf{Q}e^{\pm i\frac{qr\sqrt{1-(\hat{\mathbf{g}}\cdot\hat{\mathbf{v}})^2}}{2p}\mathbf{\Omega}}\mathbf{Q}^T \right) e^{-\frac{D\delta}{2pr^2}\tilde{\Theta}}. \quad (40)$$

Combining Eq. (40) with Eq. (37), the PGSE signal can be efficiently evaluated. Notice that all matrices involved in the resulting expression, except for the orthogonal matrix  $\mathbf{Q}$ , are diagonal. In addition, the matrix products appearing in the signal expression do not need to be formed explicitly. Since the

measured signal corresponds to the first component of the resulting coefficient vector  $\mathbf{c}(0) = [1, 0, \dots]^T$ , it is sufficient to apply the successive matrix exponentials directly to the initial vector. As a result, all operations are carried out in a matrix–vector form, which is computationally cheaper than matrix–matrix products.

This approximation was found to provide an accurate and substantially faster surrogate for repeated model evaluations for different gradient orientations. While the exact signal evaluation described in the previous sections was used to generate all results reported in the Results section, we include a dedicated subsection to compare the approximate and exact signals as a function of  $p$ , and to assess the corresponding computational speed-up, in order to evaluate the practical potential of this approach for future data-driven applications.

### 3.7 Spherical mean signal: Angular averaging and computational strategies

In many dMRI applications, it is desirable to work with observables that are invariant to the orientation of the underlying microstructure. In this context, the spherical mean (powder-averaged) dMRI signal—obtained by averaging the signal over all gradient directions<sup>47–49</sup>—provides a rotationally invariant observable that depends only on the intrinsic properties of the confining geometry and the acquisition parameters. In the present work, we therefore use the spherical mean signal to assess the behavior of the proposed model and to design efficient numerical strategies for its evaluation.

All angular averages reported in this work are computed using spherical Voronoi weights associated with the acquisition gradient directions. Specifically, given a set of unit gradient directions  $\{\mathbf{g}_i\}$ , the Voronoi-weighted spherical mean signal is computed as

$$\bar{E} = \sum_i w_i E(\mathbf{g}_i), \quad (41)$$

where the weights  $w_i$  correspond to the areas of the Voronoi cells on the unit sphere associated with each gradient direction and are normalized such that  $\sum_i w_i = 1$ . This weighted average mitigates the angular sampling bias arising from non-equidistant gradient direction sets and provides a more accurate approximation of the continuous spherical mean than uniform averaging when the acquisition scheme is not perfectly uniform.

In addition to the scheme-averaged signal, we also compute the ideal spherical mean of the proposed model, defined as the continuous angular average over the unit sphere. Owing to the axial symmetry of the cylindrical surface model in Eq. (37), the spherical mean reduces to a one-dimensional integral over  $\mu = \cos(\beta) \in [0, 1]$ :

$$\frac{\bar{E}}{E(q=0)} = \int_0^1 e^{-q^2(\Delta-\delta/3)D\mu^2} \left[ e^{-\frac{D\delta}{r^2}\tilde{\Theta}_{+i}\frac{qr\sqrt{1-\mu^2}}{2}\tilde{\mathbf{K}}} e^{-\frac{D(\Delta-\delta)}{r^2}\tilde{\Theta}} e^{-\frac{D\delta}{r^2}\tilde{\Theta}_{-i}\frac{qr\sqrt{1-\mu^2}}{2}\tilde{\mathbf{K}}} \right]_{0,0} d\mu. \quad (42)$$

This integral is evaluated by Gauss–Legendre quadrature, which provides a numerically efficient and controllable approximation of the spherical mean.

Unless otherwise stated, the exact analytical formulation derived in this work is used as numerical reference and the spherical mean is computed using the Voronoi-weighted average over the acquisition scheme. Accelerated implementations based on the Strang splitting approach described in the previous subsection and on Gauss–Legendre angular quadrature for computing the spherical mean signal are evaluated with respect to this reference in terms of accuracy and computational cost.

### 3.8 Monte Carlo simulations

Monte Carlo Diffusion Simulations (MCDS) were employed to validate the proposed analytical model. We used an MC simulator developed by our group, available at <https://github.com/ionhrafte/Robust-Monte-Carlo-Simulations><sup>50,51</sup>. This tool has been validated against analytical models across multiple geometries, including impermeable planes, cylinders, spheres, and more recently in cylindrical surfaces<sup>35</sup>.

We compared the analytical dMRI signal to those generated by the MC simulations for identical cylindrical surfaces. Specifically, dMRI signals were generated from 50 independent cylinders with radii uniformly spaced from 0.1  $\mu\text{m}$  to 5.0  $\mu\text{m}$  in increments of 0.1  $\mu\text{m}$  following the protocol described in<sup>35</sup>. The diffusion process simulation was carried out using  $N_p = 75 \times 10^3$  particles uniformly distributed on each cylindrical surface and  $N_t = 15 \times 10^3$  diffusion steps per particle. The axial myelin water diffusivity was set to  $D = 0.8 \mu\text{m}^2/\text{ms}$ , as this value produced the largest discrepancies in our previous model<sup>35</sup>.

The dMRI data were generated using a PGSE sequence with trapezoidal diffusion gradients employing a gradient strength of  $G = 500 \text{ mT/m}$  and a slew rate of  $SR = 500 \text{ T/m/s}$ , which are compatible with the specifications of a Connectome 2.0 3T scanner<sup>52</sup> and small animal 7T and 9.4T BioSpec MRI scanners. The protocol included  $90^\circ$  and  $180^\circ$  pulse durations of 2 ms and 4 ms, respectively. The data were generated for six  $b$ -values = [1, 2, 3, 4, 5, 6]  $\text{ms}/\mu\text{m}^2$ , which were selected using the shortest possible echo time (TE) for each case, while keeping the TE smaller than 20 ms and maintaining maximum  $G$  and  $SR$ , following the implementation described in<sup>53,54</sup>. For each  $b$ -value, dMRI signals were generated for 92 gradient orientations uniformly distributed on the unit sphere, along with the signal for  $b = 0$ . Table I shows the experimental parameters.

The subsequent analyses focused on the spherical mean signal normalized by the  $b = 0$  signal. The same Voronoi weights are consistently applied to analytical model evaluations and Monte Carlo simulations.

**Table I.** Experimental parameters for Monte Carlo simulations using a PGSE sequence.

$b$ -value ( $\text{ms}/\mu\text{m}^2$ )	$\Delta$ (ms)	$\delta$ (ms)	TE (ms)
1.0	7.72	2.88	13.43
2.0	8.72	3.89	15.44
3.0	9.45	4.62	16.90
4.0	10.03	5.20	18.06
5.0	10.53	5.70	19.06
6.0	10.97	6.14	19.94

## 4 Results

In this section, we first illustrate characteristic features of the diffusion signal predicted by the proposed cylindrical surface model and validate the exact analytical formulation against Monte Carlo simulations using scheme-averaged spherical mean signals computed with Voronoi weights. We then investigate the numerical accuracy and computational efficiency of the spectral formulation by analyzing its convergence with respect to the truncation order of the spectral basis and by introducing two complementary acceleration strategies based on operator splitting and angular quadrature.

### 4.1 $b$ -value-dependent spherical mean signal profile

Figure 1 illustrates the theoretical spherical mean dMRI signal arising from diffusion confined to a cylindrical surface, as predicted by the general analytical model introduced in Eq. (37). The signal was computed for a PGSE sequence with  $b$ -values ranging from 0 to 40  $\text{ms}/\mu\text{m}^2$ , and three representative cylinder radii: 1.0  $\mu\text{m}$ , 2.0  $\mu\text{m}$ , and 3.0  $\mu\text{m}$ . Additionally, we plot the spherical mean dMRI signal from the recently proposed spherical-mean Gaussian phase approximation (GPA) model for this geometry<sup>55</sup>.

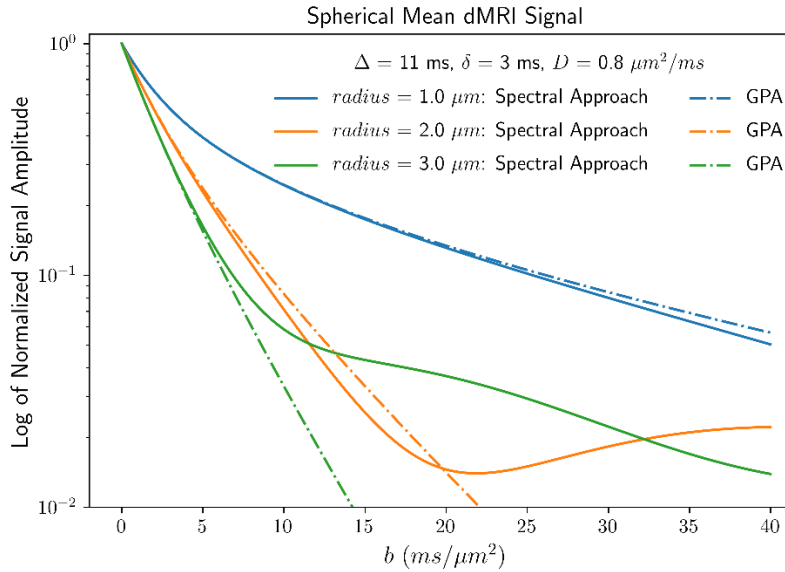


**Figure 1.** Signal attenuation for diffusion confined to cylindrical surfaces. The spherical mean dMRI signal was generated using the analytical model introduced in Eq. (37) for a PGSE sequence with  $\Delta = 11 \text{ ms}$  and  $\delta = 3 \text{ ms}$ . The axial diffusivity was set to  $D = 0.8 \mu\text{m}^2/\text{ms}$ . The signal attenuation is shown on a logarithmic scale for three cylinder radii: 1.0  $\mu\text{m}$  (blue), 2.0  $\mu\text{m}$  (orange), and 3.0  $\mu\text{m}$  (green). The analytical expression was evaluated using  $M = 50$  spectral modes (continuous lines). Additionally, we show the spherical mean signal resulting from the Gaussian Phase Approximation (GPA) model<sup>55</sup> (dashed lines). Note that the large  $b$ -values used in this figure are intended to illustrate diffraction-like patterns that are not necessarily accessible with standard clinical protocols.

For small radii (e.g.,  $r = 1.0 \mu\text{m}$ ), the GPA closely follows the exact analytical signal over a wide range of  $b$ -values, with only minor deviations appearing at very high diffusion weightings ( $b \geq 20 \text{ ms}/\mu\text{m}^2$ ). As the radius increases, however, noticeable differences between the two models emerge at lower  $b$ -values. For  $r = 2.0 \mu\text{m}$  and  $r = 3.0 \mu\text{m}$ , the GPA progressively deviates from the exact solution for  $b \geq 5 \text{ ms}/\mu\text{m}^2$ ,

with the discrepancy becoming more pronounced for larger  $b$ -values. At very high diffusion weightings, the exact solution exhibits oscillatory features commonly referred to as diffraction patterns, which arise from the angular confinement of diffusion and the resulting interference among discrete Laplacian eigenmodes on the cylindrical surface. These features are not captured by the GPA, highlighting the importance of the exact analytical formulation when describing the signal in regimes where restricted diffusion effects become dominant.

## 4.2 Validation against Monte Carlo simulations

To validate the accuracy of the proposed analytical model, we compared its predictions against MC-generated signals. Analytical signals were computed using  $M = 50$  modes.

Figure 2 shows the spherical mean dMRI signal as a function of cylinder radius for an axial diffusivity of  $D = 0.8 \mu\text{m}^2/\text{ms}$ , and six  $b$ -values ranging from 1.0 to 6.0  $\text{ms}/\mu\text{m}^2$ . The analytical model (continuous lines) exhibits excellent agreement with the MC simulations (discrete points) across the entire range of radii and  $b$ -values considered. This confirms the correctness of the spectral formulation and the exact treatment of finite gradient pulse effects.

As expected, increasing the  $b$ -value leads to stronger signal attenuation and enhanced sensitivity to the cylinder radius. For the acquisition protocol considered here, the signal displays limited sensitivity to radii smaller than approximately 0.5  $\mu\text{m}$  and larger than approximately 4.0  $\mu\text{m}$ , indicating a finite radius sensitivity window determined by the gradient strength and diffusion times of the PGSE protocol.

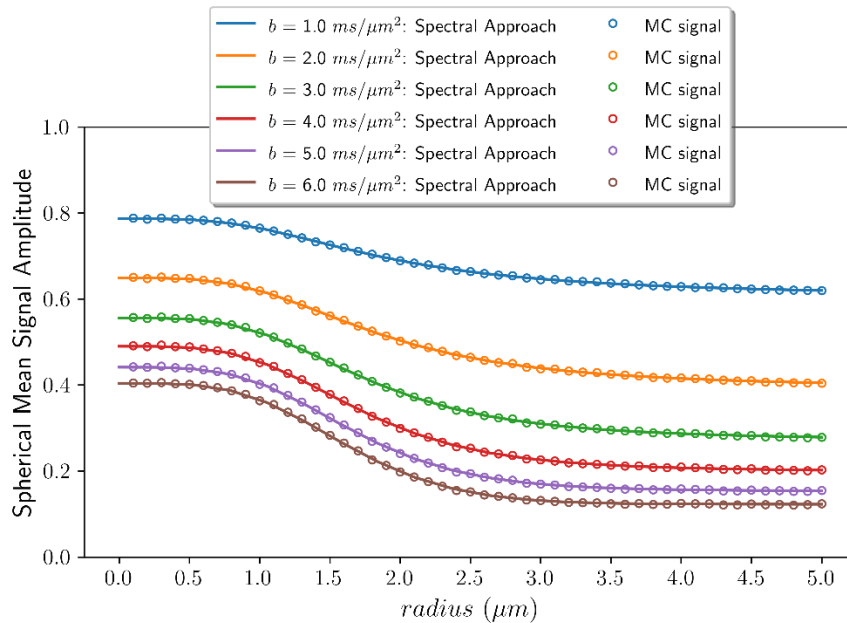


**Figure 2.** Spherical mean dMRI analytical versus MC signals. Spherical mean dMRI signals as a function of cylinder radius, computed using the analytical model (continuous lines) and Monte Carlo (MC) simulations (dots) are shown. Signals are evaluated for  $b$ -values of [1.0, 2.0, 3.0, 4.0, 5.0, 6.0]  $\text{ms}/\mu\text{m}^2$ , using a PGSE sequence with parameters listed in Table I and axial diffusivity  $D = 0.8 \mu\text{m}^2/\text{ms}$ . Analytical signals and MC simulations were generated for 50 discrete radii spanning 0–5  $\mu\text{m}$ .

### 4.3 Numerical analyses

To characterize the numerical accuracy and computational performance of the proposed analytical formulation, we investigate three independent sources of approximation error: (i) the truncation order of the spectral expansion, (ii) the number of substeps used in the Strang splitting approximation, and (iii) the number of quadrature nodes employed to evaluate the spherical mean.

In all cases, we quantify the associated accuracy-runtime trade-offs in order to assess the practical suitability of the proposed methods for repeated signal evaluations, as required in parameter estimation and fitting applications.

All experiments were performed using the same PGSE parameters  $\Delta = 10.97$  ms and  $\delta = 6.14$  ms, the same set of 92 diffusion-encoding directions used in the Monte Carlo simulations, and the same three diffusion weightings  $b = [3, 6, 20]$  ms/ $\mu\text{m}^2$ . Unless otherwise stated, the spherical mean is computed using the Voronoi-weighted average over the gradient orientations. The analysis was carried out for  $N_r=50$  independent cylinders with radii uniformly distributed between 0.1  $\mu\text{m}$  and 5.0  $\mu\text{m}$ .

For all benchmarks, execution was restricted to a single CPU core and a single thread in order to enable a fair comparison of the intrinsic computational cost, independent of hardware-specific parallelization or multi-threading effects. All computations were performed on a laptop equipped with an Intel Core i7-7700HQ CPU (8 cores, 2.80 GHz) running Linux.

#### 4.3.1 Convergence of the analytical signal with respect to the truncation order

We first investigated the convergence of the analytical signal with respect to the truncation order  $M$  of the spectral expansion. The Voronoi-weighted spherical mean computed using  $M = 50$  modes was taken as reference, denoted by  $\bar{E}_{ref}$ . Voronoi-weighted spherical mean signals  $\bar{E}_M$  computed using lower truncation orders  $M = [3, 5, 10, 20]$  were compared against this reference.

For each truncation order and each  $b$ -value, the total signal discrepancy over all  $N_r=50$  radii was quantified using the mean relative absolute error (MRAE), defined as

$$MRAE_M = \frac{1}{N_r} \sum_{i=1}^{N_r} \frac{|\bar{E}_M(r_i) - \bar{E}_{ref}(r_i)|}{\bar{E}_{ref}(r_i)} \cdot 100\%. \quad (43)$$

In addition, we report the computation time required to generate the Voronoi-weighted spherical mean signal for all gradient directions per radius, together with the corresponding acceleration factor relative to the reference computation using  $M=50$  modes. For comparison, we also include the results obtained from the spherical-mean GPA model<sup>55</sup>. The resulting accuracy and performance metrics are summarized in Table II.

The results demonstrate very rapid convergence of the analytical signal with respect to the truncation order. In particular,  $M=10$  already yields results that are numerically indistinguishable from those obtained with substantially higher truncation orders, while even  $M=5$  provides accurate approximations under the present acquisition conditions. This confirms that only a limited number of angular modes

contribute significantly to the signal, since the quadratic growth of the Laplace eigenvalues strongly suppresses higher-order contributions.

For comparison, the spherical-mean GPA model provides the shortest computation time, yielding an acceleration factor of approximately  $4.8 \times 10^3$  relative to the reference calculation. However, this gain in speed comes at the cost of substantially larger relative absolute errors, exceeding those obtained even with very low truncation orders (e.g.,  $M = 3$ ).

**Table II.** Mean relative absolute error (*MRAE*), computation time and acceleration factor as a function of the truncation order  $M$  of the spectral expansion. The *MRAE* and acceleration factor are computed with respect to the Voronoi-weighted spherical mean signal obtained with  $M = 50$  modes. Reported computation times correspond to the average time required to generate the Voronoi-weighted spherical mean signal over the 92 diffusion-encoding directions for a single cylinder radius and  $b$ -value. The average was computed by dividing the total runtime for all 50 radii and three diffusion weightings by  $50 \times 3$ . Results are reported for three diffusion weightings:  $b = [3, 6, 20]$   $\text{ms}/\mu\text{m}^2$ . Results from the spherical mean Gaussian phase approximation (GPA) model are also included.

Truncation order	<i>MRAE</i> (100%)			Computation time ( <i>milliseconds</i> )	Acceleration factor ( $\times$ )
	$b = 3.0 \text{ ms}/\mu\text{m}^2$	$b = 6.0 \text{ ms}/\mu\text{m}^2$	$b = 20 \text{ ms}/\mu\text{m}^2$		
$M = 3$	$4.1 \times 10^{-3}$	$6.2 \times 10^{-2}$	4.5	9.8 ms	11.3
$M = 5$	$2.7 \times 10^{-7}$	$2.4 \times 10^{-5}$	$5.1 \times 10^{-2}$	10.2 ms	10.9
$M = 10$	$3.8 \times 10^{-11}$	$1.8 \times 10^{-11}$	$2.5 \times 10^{-10}$	12.5 ms	8.9
$M = 20$	$3.4 \times 10^{-11}$	$2.4 \times 10^{-11}$	$3.2 \times 10^{-11}$	18.5 ms	6.0
$M = 50$	<i>Reference</i>	<i>Reference</i>	<i>Reference</i>	111.0 ms	<i>Reference</i>
GPA	3.05	14.6	60.0	0.023 ms	$4.8 \times 10^3$

#### 4.3.2 Convergence of the approximated signal with respect to the Strang splitting

Next, we assessed the convergence properties of the approximated analytical signal obtained using the Strang splitting approach as a function of the number of substeps  $p$ .

As reference, we used the Voronoi-weighted spherical mean signal generated with the exact analytical model using  $M=10$  modes, which was selected based on the convergence analysis of the previous subsection. Approximated signals computed using  $p = [5, 10, 20, 40, 80]$  substeps were compared against this reference.

The analysis was performed for the same set of 50 cylinder radii and the same three  $b$ -values. For each value of  $p$ , the overall discrepancy with respect to the reference signal was quantified using the *MRAE*. In addition, we report the corresponding computation times and acceleration factors relative to the exact analytical evaluation. The results are reported in Table III.

**Table III.** Mean relative absolute error (*MRAE*), computation time and acceleration factor as a function of the number of Strang splitting substeps  $p$ . The *MRAE* and acceleration factor are computed with respect to the exact analytical signal generated with  $M = 10$  modes. Reported computation times correspond to the average time required to generate the Voronoi-weighted spherical mean signal over the 92 diffusion-encoding directions for a single cylinder radius and  $b$ -value. The average was computed by dividing the total runtime for all 50 radii and three diffusion weightings by  $50 \times 3$ . Results are reported for three diffusion weightings:  $b = [3, 6, 20]$  ms/ $\mu\text{m}^2$ .

Splitting substeps	<i>MRAE</i> (100%)			Computation time ( <i>milliseconds</i> )	Acceleration factor ( $\times$ )
	$b = 3.0$ ms/ $\mu\text{m}^2$	$b = 6.0$ ms/ $\mu\text{m}^2$	$b = 20$ ms/ $\mu\text{m}^2$		
$p = 5$	0.55	1.01	2.0	0.6 ms	20.8
$p = 10$	0.14	0.26	0.53	0.8 ms	15.6
$p = 20$	0.036	0.065	0.135	1.3 ms	9.6
$p = 40$	0.009	0.016	0.034	2.2 ms	5.7
$p = 80$	0.002	0.004	0.009	4.1 ms	3.0

The results in Table III show that the Strang splitting approximation achieves high accuracy with a relatively moderate number of substeps, while substantially reducing the computational cost. For example, for  $p = 20$  the *MRAE* is below 0.2% across all diffusion weightings, while the computation is approximately one order of magnitude faster than the exact evaluation. For  $p = 40$ , the approximated signals are visually indistinguishable from the exact signals (results not shown).

As expected, a small number of substeps leads to noticeable approximation errors, particularly at higher diffusion weightings, highlighting the need for a minimal number of substeps when operating in high- $b$  regimes.

#### 4.3.3 Convergence of the spherical mean with respect to quadrature nodes

Since the spherical mean constitutes a central observable in many applications, we investigated the convergence properties of the spherical mean signal computed by Gauss–Legendre quadrature.

All signals in this experiment were generated using the exact analytical model with  $M = 10$  modes. The reference signal was taken as the scheme-averaged signal computed using Voronoi weights for the 92 diffusion-encoding directions. This reference was compared with the spherical mean obtained by Gauss–Legendre quadrature using  $n_q = [5, 6, 7, 8, 20]$  nodes.

For each value of  $n_q$  and each  $b$ -value, the discrepancy with respect to the Voronoi-weighted spherical mean was quantified using the *MRAE* over all 50 radii employed in the previous sections. The corresponding computation times and acceleration factors are reported in Table IV.

**Table IV.** Mean relative absolute error (*MRAE*), computation time and acceleration factor as a function of the number of quadrature nodes  $n_q$  used in the Gauss–Legendre integration. All signals were generated using the exact analytical model with  $M = 10$  modes. The *MRAE* and acceleration factor are computed with respect to the Voronoi-weighted scheme-averaged signal obtained using 92 diffusion-encoding directions. Reported computation times correspond to the average time required to generate the Voronoi-weighted spherical mean signal over the 92 diffusion-encoding directions for a single cylinder radius and  $b$ -value. The average was computed by dividing the total runtime for all 50 radii and three diffusion weightings by  $50 \times 3$ . Results are reported for three diffusion weightings:  $b = [3, 6, 20]$  ms/ $\mu\text{m}^2$ .

Quadrature nodes	<i>MRAE</i> (100%)			Computation time ( <i>milliseconds</i> )	Acceleration factor ( $\times$ )
	$b = 3.0$ ms/ $\mu\text{m}^2$	$b = 6.0$ ms/ $\mu\text{m}^2$	$b = 20$ ms/ $\mu\text{m}^2$		
$n_q = 5$	0.0262	0.0777	0.5867	0.7 ms	17.9
$n_q = 6$	0.0262	0.0776	0.6282	0.9 ms	13.9
$n_q = 7$	0.0262	0.0776	0.6529	1.0 ms	12.5
$n_q = 8$	0.0262	0.0776	0.6481	1.2 ms	10.4
$n_q = 20$	0.0262	0.0776	0.6485	2.8 ms	4.5

The results demonstrate stable and rapid convergence of the Gauss–Legendre quadrature with respect to the number of nodes. Very similar accuracy is observed for  $n_q$  between 5 and 20, indicating that a number of quadrature nodes substantially smaller than the number of diffusion-encoding directions can be used in practice. This enables a significant reduction in the computational cost of spherical mean evaluation, without requiring the explicit generation of the signal for each experimental gradient direction.

After evaluating the individual acceleration strategies in this and previous sections, we finally assess their combined impact on the computation of the spherical mean signal. To this end, we performed a representative experiment in which the spherical mean analytical signal was generated using a truncation order of  $M = 10$ , evaluated through the Strang splitting approach with  $p = 10$  steps and  $n_q = 5$  Gauss–Legendre quadrature nodes. Under these settings, the resulting *MRAE* values for the three considered diffusion weightings (i.e.,  $b = [3, 6, 20]$  ms/ $\mu\text{m}^2$ ) were [0.17, 0.34, 1.11], respectively. The average computation time was 0.031 ms per cylinder radius and  $b$ -value. The implementation was further accelerated by compiling the numerical routines using the just-in-time Numba compiler<sup>56</sup>.

Comparing these results with those obtained from the GPA model reported in Table II for the same acquisition parameters shows that the computational cost of the accelerated analytical formulation is of the same order of magnitude as that of the GPA (i.e., 0.031 ms vs 0.028 ms), while yielding substantially smaller approximation errors.

## 5 Discussion

The main result of this work is the exact analytical solution of the Bloch–Torrey equation for diffusion confined to a cylindrical surface under finite PGSE gradients, yielding a closed-form expression for the corresponding dMRI signal valid for arbitrary gradient durations and separations. Notably, this solution does not rely on assumptions on the propagator, spin phase distribution, or finite-pulse effects. Related spectral approaches have been reported in the literature for restricted diffusion inside cylinders and spheres, and between parallel planes with reflecting boundaries<sup>20,21,24,29,57</sup>.

The only approximation involved in the practical evaluation of the signal expression is numerical, due to the truncation of the spectral basis. This truncation is well controlled, as the eigenvalues of the Laplace operator on the cylindrical surface grow quadratically with the mode index, leading to rapid convergence of the series. As a result, the analytical signal can be evaluated with high accuracy using a relatively small number of spectral modes (e.g.,  $M = 10$ ; see Table II). The proposed analytical signal expression was validated against Monte Carlo diffusion simulations over a wide range of cylinder radii and PGSE parameters (see Figure 2).

For the geometry under study, the diffusion process is constrained along the (periodic) angular coordinate while remaining unbounded along the cylinder’s main axis. This leads to a natural decoupling of the diffusive motion into perpendicular and parallel components, reflected in the factorized structure of the signal. We significantly reduced the dimensionality of the matrices involved in the signal evaluation by exploiting the symmetry of the cylindrical surface and introducing a reduced real spectral basis, thus achieving computational gains without compromising accuracy.

Beyond the exact analytical formulation, an additional contribution of this work is the introduction of efficient numerical strategies that enable fast and repeated evaluations of the proposed signal model. In particular, we introduced a second-order Strang splitting approximation for the matrix exponential operators arising in the PGSE signal expression, which allows the time evolution to be decomposed into a sequence of simpler operators that can be efficiently applied through a precomputed eigendecomposition. This approach avoids repeated evaluations of dense matrix exponentials and enables the signal to be computed by a sequence of matrix–vector operations, yielding substantial computational savings while preserving a controllable approximation error (see Table III). In addition, we proposed an efficient evaluation of the spherical mean (powder-averaged) signal based on Gauss–Legendre quadrature, exploiting the axial symmetry of the cylindrical surface model to reduce the angular integration to a one-dimensional quadrature problem (see Table IV). Together, these developments provide a practical framework for accelerating both the evaluation of the directional signal and the computation of rotationally invariant observables, which are of central interest in many dMRI applications and in parameter estimation problems requiring repeated model evaluations.

The numerical analyses presented in this work further clarify the accuracy–efficiency trade-offs associated with these approximations. Although the results show that relatively small truncation orders of the spectral expansion and a moderate number of Strang splitting substeps are sufficient to achieve high accuracy for the PGSE protocol considered here, these numerical parameters should not be adopted indiscriminately. In practical applications, the required truncation order depends on the acquisition parameters and on the range of cylinder radii of interest, and a dedicated convergence analysis should therefore be carried out for each specific particular application. Likewise, the convergence of the Strang splitting approximation depends on the temporal structure and strength of the diffusion-encoding

gradients, so that an application-specific assessment is needed to identify an appropriate number of splitting substeps that balances accuracy and computational efficiency. Finally, the Voronoi-weighted powder average and the Gauss–Legendre evaluation of the spherical mean correspond to two distinct numerical approximations of angular averaging. While the Voronoi-based approach provides a protocol-consistent estimate of the powder-averaged signal for a finite and potentially non-uniform set of diffusion-encoding directions, the Gauss–Legendre quadrature approximates the continuous, rotationally invariant spherical mean of the model. As a result, these two quantities do not necessarily coincide for a given acquisition scheme, and their differences reflect the finite and possibly non-uniform angular sampling of the protocol.

In a previous study, we derived an exact analytical expression for diffusion constrained to cylindrical surfaces in the narrow-pulse limit and proposed an approximate extension to finite gradient durations<sup>35</sup>. While that formulation captured the main features of surface-confined diffusion and showed good agreement with Monte Carlo simulations in various regimes, discrepancies emerged for large diffusivities and high diffusion weightings, where finite-pulse and non-Gaussian effects become non-negligible. Recently, a new extension for wide pulses based on the Gaussian phase approximation was introduced in<sup>55</sup>, which yields accurate results for relatively small radii. The present work overcomes previous limitations by providing an exact treatment of finite gradient pulse durations, thereby completing the theoretical description presented in previous works.

From a broader theoretical perspective, a general spectral approach was developed to describe restricted diffusion in circular layers of arbitrary thickness under time-dependent gradient fields<sup>27</sup>. Within such a framework, diffusion confined to a cylindrical surface can be formally interpreted as a limiting case corresponding to a vanishing radial layer thickness. Therefore, our work could be rederived following the theoretical treatment presented in<sup>27</sup>. However, rather than relying on this implicit limit, the present work follows a direct derivation tailored to the surface geometry. This strategy enables the explicit construction of the spectral geometry-specific matrices governing the PGSE signal and yields a compact analytical expression that is particularly suited for practical signal evaluation.

The present formulation relies on a number of idealizations that define its domain of applicability. The cylinder is assumed to be infinitely long, thereby neglecting end effects. The surface is treated as perfectly smooth and impermeable, and no exchange with other compartments is considered. In addition, relaxation effects and surface relaxivity are not explicitly included in the model. While these assumptions are appropriate for isolating the effect of surface confinement on the diffusion signal, they should be kept in mind when considering applications to biological tissues or more complex geometries. The analytical framework developed here can be extended in several directions. Possible extensions include the incorporation of distributions of (concentric) cylinder radii, alternative gradient waveforms, and additional physical effects such as relaxation or exchange.

The presented model can be extended to arbitrary waveforms following the approach described in<sup>20,21,30</sup>. That is, by dividing the time interval of the waveform into small subintervals and approximating the waveform by a piecewise constant function in each subinterval. The optimal number of subintervals depends on the smoothness of the waveform. For example, a PGSE experiment with trapezoidal gradients would require at least seven subintervals to represent the full waveform, including the rising and falling ramps of the two diffusion gradients, the two plateau intervals at constant gradient amplitude, and the interval in which the gradient is zero. In practice, a finer subdivision of the ramp intervals may be required depending on the slew rate and on the desired accuracy of the waveform approximation. The resulting signal would involve the multiplication of the matrix exponentials corresponding to each of the

subintervals in which the waveform is assumed to be constant. As a result, although the practical implementation is straightforward, the computation time grows proportionally with the number of subintervals.

For this reason, we focused on rectangular PGSE gradients, as they involve three distinct subintervals and allow an exact analytical treatment. In modern scanners with high slew rates, the ramp durations of trapezoidal gradients are short compared to the pulse duration, so their impact on the resulting diffusion signal is relatively small. As a result, trapezoidal gradients produce signals that are very well approximated by those from rectangular gradients with the same nominal timing parameters  $(\Delta, \delta)$ . Consistent with this, the signals generated by the proposed analytical model were in excellent agreement with those obtained from Monte Carlo simulations using trapezoidal gradients (see Table I and Figure 2).

While the cylindrical surface model is motivated by applications to myelin water diffusion<sup>35,36,54,55,58–60</sup>, this work focuses on the theoretical formulation of the dMRI signal model, establishing a rigorous foundation for future experimental and data-driven studies. Closed-form analytical solutions of the Bloch–Torrey equation under finite gradient pulses are available only for a limited number of geometries. The present result extends this class to diffusion confined to cylindrical surfaces.

### **Data availability statement**

The datasets and code supporting the findings of this study are publicly available at the following repository: <https://github.com/ejcanalesr/exact-PGSE-dMRI-signal-cylindrical-surface>.

### **Author contributions**

EC-R: Conceptualization, Investigation, Methodology, Project administration, Data curation, Formal Analysis, Resources, Software, Supervision, Validation, Visualization, Writing—original draft, Writing—review and editing. CT: Investigation, Software, Validation, Visualization, Writing—review and editing. JM-G: Investigation, Resources, Writing—review and editing. DJ: Investigation, Resources, Writing—review and editing. J-PT: Investigation, Resources, Writing—review and editing. JR-P: Investigation, Methodology, Data curation, Formal Analysis, Resources, Software, Validation, Visualization, Writing—original draft, Writing—review and editing.

### **Acknowledgments**

E.J.C.R. acknowledges financial support from the “Ramón y Cajal” Excellence Fellowship (Grant [RYC2023-042763-I](#)), funded by the Ministry of Science, Innovation and Universities (MICIU) and the Spanish State Research Agency (AEI, 10.13039/50110001103), and co-financed by the European Social Fund Plus (ESF+).

## Conflict of interest

The authors declare that the research was conducted without any commercial or financial relationships that could be construed as a potential conflict of interest.

## Generative AI statement

The authors declare that ChatGPT-5.2 (paid version) was used to assist in identifying grammatical errors and typos in this manuscript. All intellectual contributions were made by the authors.

## Appendices

### Appendix A: Computing matrix B

The integral in Eq. (17) is solved as:

$$\begin{aligned} B_{nm} &= \left( \frac{1}{2\pi} \right) r \int_0^{2\pi} \cos(\theta) e^{in\theta} e^{-im\theta} d\theta \\ &= \left( \frac{1}{2\pi} \right) r \int_0^{2\pi} \cos(\theta) e^{i(n-m)\theta} d\theta \\ &= \left( \frac{1}{2\pi} \right) \frac{r}{2} \int_0^{2\pi} (e^{i\theta} + e^{-i\theta}) e^{i(n-m)\theta} d\theta \\ &= \left( \frac{1}{2\pi} \right) \frac{r}{2} \left( \int_0^{2\pi} e^{i(n-(m-1))\theta} d\theta + \int_0^{2\pi} e^{i(n-(m+1))\theta} d\theta \right), \end{aligned} \tag{44}$$

where we used Euler's formula. Without loss of generality, here we assumed that the diffusion gradient is applied along the x-axis (assuming the cylinder's axis is parallel to the z-axis). Therefore, the angle between the gradient and the position vector is  $\theta$ . Note this assumption does not affect the dMRI signal  $E_{\perp}$ , since it is constant for any gradient orientation lying on the plane perpendicular to the cylinder's axis.

The above integrals can be evaluated by using the identity:

$$\int_0^{2\pi} e^{i(n-m)\theta} d\theta = 2\pi \delta_{n,m} . \tag{45}$$

Thus,

$$B_{nm} = \frac{r}{2} (\delta_{n,m-1} + \delta_{n,m+1}). \tag{46}$$

### Appendix B: Proving the relationship in Eq. (27)

The transformation matrix in Eq. (25) satisfy the following properties:  $\mathbf{T}^T \mathbf{T} = \mathbf{I}$  is the identity and

$$\mathbf{T}\mathbf{T}^T = \begin{bmatrix} 1/2 & \cdots & 0 & 0 & 0 & \cdots & 1/2 \\ \vdots & \ddots & & \vdots & & \ddots & \vdots \\ 0 & & 1/2 & 0 & 1/2 & & 0 \\ 0 & \cdots & 0 & 1 & 0 & \cdots & 0 \\ 0 & & 1/2 & 0 & 1/2 & & 0 \\ \vdots & \ddots & & \vdots & & \ddots & \vdots \\ 1/2 & \cdots & 0 & 0 & 0 & \cdots & 1/2 \end{bmatrix}. \quad (47)$$

Note that for a symmetric matrix  $\mathbf{A}$ , we get the following equality:  $\mathbf{A}\mathbf{T} = \mathbf{T}(\mathbf{T}^T\mathbf{A}\mathbf{T})$ . This can be demonstrated by multiplying both sides of the equation by  $\mathbf{T}^T$ , from the left, and replacing  $\mathbf{T}^T\mathbf{T}$  by the identity matrix.

The relationship we want to simplify is  $\mathbf{T}^T e^{-\mathbf{A}_3} e^{-\mathbf{A}_2} e^{-\mathbf{A}_1} \mathbf{T}$ . For this, let's first write the matrix exponential in Taylor series:

$$e^{-\mathbf{A}} = \sum_{k=0}^{\infty} \frac{(-1)^k}{k!} \mathbf{A}^k = \mathbf{I} - \mathbf{A} + \frac{1}{2!} \mathbf{A}^2 - \frac{1}{3!} \mathbf{A}^3 + \dots \quad (48)$$

After substituting this relationship into the term  $e^{-\mathbf{A}_1}$  we get

$$\begin{aligned} \mathbf{T}^T e^{-\mathbf{A}_3} e^{-\mathbf{A}_2} e^{-\mathbf{A}_1} \mathbf{T} &= \mathbf{T}^T e^{-\mathbf{A}_3} e^{-\mathbf{A}_2} \left( \sum_{k=0}^{\infty} \frac{(-1)^k}{k!} \mathbf{A}_1^k \mathbf{T} \right), \\ &= \mathbf{T}^T e^{-\mathbf{A}_3} e^{-\mathbf{A}_2} \mathbf{T} \left( \sum_{k=0}^{\infty} \frac{(-1)^k}{k!} (\mathbf{T}^T \mathbf{A}_1 \mathbf{T})^k \right) \\ &= \mathbf{T}^T e^{-\mathbf{A}_3} e^{-\mathbf{A}_2} \mathbf{T} e^{-\mathbf{T}^T \mathbf{A}_1 \mathbf{T}}. \end{aligned} \quad (49)$$

In the previous derivation, we used the relationship

$$\mathbf{A}^k \mathbf{T} = \mathbf{T} (\mathbf{T}^T \mathbf{A} \mathbf{T})^k, \quad (50)$$

which can be obtained by doing the following iterative algebraic substitutions,  $\mathbf{A}^{k-1} \mathbf{A} \mathbf{T} = \mathbf{A}^{k-1} \mathbf{T} (\mathbf{T}^T \mathbf{A} \mathbf{T}) = \mathbf{A}^{k-2} \mathbf{A} \mathbf{T} (\mathbf{T}^T \mathbf{A} \mathbf{T}) = \mathbf{A}^{k-2} \mathbf{T} (\mathbf{T}^T \mathbf{A} \mathbf{T})^2 \dots = \mathbf{A}^{k-p} \mathbf{T} (\mathbf{T}^T \mathbf{A} \mathbf{T})^p$ , until  $p = k$ .

We can apply the same procedure to those matrix exponentials involving  $\mathbf{A}_2$  and  $\mathbf{A}_3$ , respectively, and Eq. (49) becomes

$$\begin{aligned} \mathbf{T}^T e^{-\mathbf{A}_3} e^{-\mathbf{A}_2} e^{-\mathbf{A}_1} \mathbf{T} &= \mathbf{T}^T e^{-\mathbf{A}_3} \mathbf{T} e^{-\mathbf{T}^T \mathbf{A}_2 \mathbf{T}} e^{-\mathbf{T}^T \mathbf{A}_1 \mathbf{T}} \\ &= \mathbf{T}^T \mathbf{T} e^{-\mathbf{T}^T \mathbf{A}_3 \mathbf{T}} e^{-\mathbf{T}^T \mathbf{A}_2 \mathbf{T}} e^{-\mathbf{T}^T \mathbf{A}_1 \mathbf{T}} \\ &= e^{-\mathbf{T}^T \mathbf{A}_3 \mathbf{T}} e^{-\mathbf{T}^T \mathbf{A}_2 \mathbf{T}} e^{-\mathbf{T}^T \mathbf{A}_1 \mathbf{T}}. \end{aligned} \quad (51)$$

To obtain the expression in Eq. (28), we substituted matrices  $\mathbf{A}_1 = (D\mathbf{\Lambda} + i\gamma\mathbf{GB})\delta$ ,  $\mathbf{A}_2 = D(\mathbf{\Lambda} - \delta)\mathbf{\Lambda}$ , and  $\mathbf{A}_3 = (D\mathbf{\Lambda} - i\gamma\mathbf{GB})\delta$  in Eq. (51) with the matrices in the matrix exponential terms in Eq. (26), which are symmetric.

## References

1. Mitra PP, Sen PN. Effects of microgeometry and surface relaxation on NMR pulsed-field- gradient experiments: Simple pore geometries. *Phys Rev B*. 1992;45(1):143-156. doi:10.1103/PHYSREVB.45.143
2. Le Bihan D. The “wet mind”: water and functional neuroimaging. *Phys Med Biol*. 2007;52(7):R57-90. doi:S0031-9155(07)80522-7 [pii]10.1088/0031-9155/52/7/R02
3. Brownstein KR, Tarr CE. Importance of classical diffusion in NMR studies of water in biological cells. *Phys Rev A*. 1979;19(6):2446-2453. doi:10.1103/PhysRevA.19.2446
4. Basser PJ, Mattiello J, LeBihan D. MR diffusion tensor spectroscopy and imaging. *Biophys J*. 1994;66(1):259-267. doi:S0006-3495(94)80775-1 [pii]10.1016/S0006-3495(94)80775-1
5. Stejskal EO, Tanner JE. Spin Diffusion Measurements: Spin Echoes in the Presence of a Time-Dependent Field Gradient. *J Chem Phys*. 1965;42(1):288. doi:10.1063/1.1695690
6. Novikov DS, Kiselev VG, Jespersen SN. On modeling. *Magn Reson Med*. 2018;79(6):3172-3193. Accessed September 11, 2018. <http://doi.wiley.com/10.1002/mrm.27101>
7. Alexander DC, Dyrby TB, Nilsson M, Zhang H. Imaging brain microstructure with diffusion MRI: practicality and applications. *NMR Biomed. John Wiley & Sons, Ltd*. 2019;32(4):e3841. doi:10.1002/nbm.3841
8. Dyrby TB, Innocenti GM, Bech M, Lundell H. *Validation Strategies for the Interpretation of Microstructure Imaging Using Diffusion MRI*. Vol 182.; 2018:62-79.
9. Canales-Rodríguez EJ, Pizzolato M, Zhou FL, et al. Pore size estimation in axon-mimicking microfibers with diffusion-relaxation MRI. *Magn Reson Med*. Published online 2024. doi:10.1002/MRM.29991
10. Barakovic M, Pizzolato M, Tax CMW, et al. Estimating axon radius using diffusion-relaxation MRI: calibrating a surface-based relaxation model with histology. *Front Neurosci*. 2023;17:1209521. doi:10.3389/FNINS.2023.1209521
11. Veraart J, Nunes D, Rudrapatna U, et al. Noninvasive quantification of axon radii using diffusion MRI. *Elife*. 2020;9. doi:10.7554/eLife.49855
12. Jones DK, Alexander DC, Bowtell R, et al. Microstructural imaging of the human brain with a “super-scanner”: 10 key advantages of ultra-strong gradients for diffusion MRI. *Neuroimage*. Published online May 22, 2018. doi:10.1016/j.neuroimage.2018.05.047
13. Alexander DC, Hubbard PL, Hall MG, et al. Orientationally invariant indices of axon diameter and density from diffusion MRI. *Neuroimage*. 2010;52(4):1374-1389. doi:S1053-8119(10)00775-5 [pii]10.1016/j.neuroimage.2010.05.043

14. Palombo M, Ianus A, Guerreri M, et al. SANDI: A compartment-based model for non-invasive apparent soma and neurite imaging by diffusion MRI. *Neuroimage*. 2020;215. doi:10.1016/J.NEUROIMAGE.2020.116835
15. Jelescu IO, Palombo M, Bagnato F, Schilling KG. Challenges for biophysical modeling of microstructure. *J Neurosci Methods*. 2020;344:108861. doi:10.1016/J.JNEUMETH.2020.108861
16. Özarslan E, Shemesh N, Basser PJ, Ozarslan E, Shemesh N, Basser PJ. A general framework to quantify the effect of restricted diffusion on the NMR signal with applications to double pulsed field gradient NMR experiments. *J Chem Phys*. 2009;130(10):104702. doi:10.1063/1.3082078
17. Grebenkov DS. Pulsed-gradient spin-echo monitoring of restricted diffusion in multilayered structures. *J Magn Reson*. 2010;205(2):181-195. doi:10.1016/j.jmr.2010.04.017S1090-7807(10)00119-9 [pii]
18. Nilsson M, Lasič S, Drobnjak I, et al. Resolution limit of cylinder diameter estimation by diffusion MRI: The impact of gradient waveform and orientation dispersion. *NMR Biomed*. 2017;30(7). doi:10.1002/nbm.3711
19. Robertson B. Spin-echo decay of spins diffusing in a bounded region. *Phys Rev*. 1966;151(1):273-277. doi:10.1103/PhysRev.151.273
20. Caprihan A, Wang LZ, Fukushima E. A Multiple-Narrow-Pulse Approximation for Restricted Diffusion in a Time-Varying Field Gradient. *J Magn Reson Ser A*. 1996;118(1):94-102. doi:10.1006/JMRA.1996.0013
21. Callaghan PT. A simple matrix formalism for spin echo analysis of restricted diffusion under generalized gradient waveforms. *J Magn Reson*. 1997;129(1):74-84. doi:S1090-7807(97)91233-7 [pii]10.1006/jmre.1997.1233
22. Callaghan PT, Codd SL. Generalised calculation of NMR imaging edge effects arising from restricted diffusion in porous media. *Magn Reson Imaging*. 1998;16(5-6):471-478. doi:S0730-725X(98)00070-8 [pii]
23. Codd SL, Callaghan PT. Spin Echo Analysis of Restricted Diffusion under Generalized Gradient Waveforms: Planar, Cylindrical, and Spherical Pores with Wall Relaxivity. *J Magn Reson*. 1999;137(2):358-372. doi:10.1006/jmre.1998.1679S1090-7807(98)91679-2 [pii]
24. Barzykin A V. Theory of Spin Echo in Restricted Geometries under a Step-wise Gradient Pulse Sequence. *J Magn Reson*. 1999;139(2):342-353.
25. Axelrod S, Sen PN. Nuclear magnetic resonance spin echoes for restricted diffusion in an inhomogeneous field: Methods and asymptotic regimes. *J Chem Phys*. 2001;114(15):6878-6895. doi:10.1063/1.1356010
26. Grebenkov DS. Multiexponential attenuation of the CPMG spin echoes due to a geometrical confinement. *J Magn Reson*. 2006;180(1):118-126. doi:10.1016/J.JMR.2006.01.014
27. Grebenkov DS. Analytical solution for restricted diffusion in circular and spherical layers under inhomogeneous magnetic fields. *J Chem Phys*. 2008;128(13):134702. doi:10.1063/1.2841367
28. Grebenkov DS. NMR survey of reflected Brownian motion. *Rev Mod Phys*. 2007;79(3):1077-1137. doi:10.1103/REVMODPHYS.79.1077/P1077\_1\_EQ2.TIFF/MEDIUM

29. Grebenkov DS. Laplacian eigenfunctions in NMR. I. A numerical tool. *Concepts Magn Reson Part A*. 2008;32A(4):277-301. doi:10.1002/cmr.a.20117
30. Grebenkov DS. Laplacian eigenfunctions in NMR. II. Theoretical advances. *Concepts Magn Reson Part A*. 2009;34A(5):264-296. doi:10.1002/CMR.A.20145
31. Lori NF, Conturo TE, Le Bihan D. Definition of displacement probability and diffusion time in q-space magnetic resonance measurements that use finite-duration diffusion-encoding gradients. *J Magn Reson*. 2003;165(2):185-195. doi:S1090780703002805 [pii]
32. van Gelderen P, Despres D, van Zijl PC, et al. Evaluation of restricted diffusion in cylinders. Phosphocreatine in rabbit leg muscle. *J Magn Reson B*. 1994;103(3):255-260. doi:10.1006/JMRB.1994.1038
33. Balinov B, Jönsson B, Linse P, Söderman O. The NMR self-diffusion method applied to restricted diffusion. Simulation of echo attenuation from molecules in spheres and between planes. *J Magn Reson A*. 1993;104:17-25.
34. Söderman O, Jönsson B. Restricted diffusion in cylindrical geometry. *J Magn Reson*. 1995;Series A,:94-97.
35. Canales-Rodríguez EJ, Tax CMW, Fisch-Gomez E, Jones DK, Thiran JP, Rafael-Patiño J. A diffusion MRI model for random walks confined on cylindrical surfaces: towards non-invasive quantification of myelin sheath radius. *Front Phys*. 2025;13:1516630. doi:10.3389/fphy.2025.1516630
36. Peled S, Cory DG, Raymond SA, Kirschner DA, Jolesz FA. Water Diffusion, T2, and Compartmentation in Frog Sciatic Nerve. *Magn Reson Med*. 1999;42(5):911. doi:10.1002/(sici)1522-2594(199911)42:5<911::aid-mrm11>3.0.co;2-j
37. Inouye H, Kirschner DA. Evolution of myelin ultrastructure and the major structural myelin proteins. *Brain Res*. 2016;1641:43-63. doi:10.1016/J.BRAINRES.2015.10.037
38. Inouye H, Kuo FH, Denninger AR, Weinhausen B, Burghammer M, Kirschner DA. Myelin structure in unfixed, single nerve fibers: Scanning X-ray microdiffraction with a beam size of 200 nm. *J Struct Biol*. 2017;200(3):229-243. doi:10.1016/J.JSB.2017.07.001
39. Barzykin A. Exact solution of the Torrey-Bloch equation for a spin echo in restricted geometries. *Phys Rev B*. 1998;58(21):14171. doi:10.1103/PhysRevB.58.14171
40. Torrey HC. Bloch Equations with Diffusion Terms. *Phys Rev*. 1956;104(3):563-565. doi:10.1103/PhysRev.104.563
41. Griffiths DJ., Schroeter DF. *Introduction to Quantum Mechanics*. Third edit. Cambridge University Press; 2018.  
[https://www.librarysearch.manchester.ac.uk/discovery/fulldisplay?vid=44MAN\\_INST:MU\\_NUI&t=ab=local&docid=alma992979324700501631&lang=en&context=L](https://www.librarysearch.manchester.ac.uk/discovery/fulldisplay?vid=44MAN_INST:MU_NUI&t=ab=local&docid=alma992979324700501631&lang=en&context=L)
42. Higham NJ. The Scaling and Squaring Method for the Matrix Exponential Revisited. <https://doi.org/10.1137/04061101X>. 2006;26(4):1179-1193. doi:10.1137/04061101X
43. Al-Mohy AH, Higham NJ. A New Scaling and Squaring Algorithm for the Matrix Exponential. <https://doi.org/10.1137/09074721X>. 2009;31(3):970-989. doi:10.1137/09074721X

44. Assaf Y, Freidlin RZ, Rohde GK, Basser PJ. New modeling and experimental framework to characterize hindered and restricted water diffusion in brain white matter. *Magn Reson Med*. 2004;52(5):965-978. doi:10.1002/mrm.20274
45. Strang G. On the Construction and Comparison of Difference Schemes. <https://doi.org/10.1137/0705041>. 2006;5(3):506-517. doi:10.1137/0705041
46. Marchuk GI. Some application of splitting-up methods to the solution of mathematical physics problems. *Appl Mat*. 13(2):103-132.
47. Edén M. Computer simulations in solid-state NMR. III. Powder averaging. *Concepts Magn Reson Part A*. 2003;18A(1):24-55. doi:10.1002/CMR.A.10065
48. Lasič S, Szczepankiewicz F, Eriksson S, Nilsson M, Topgaard D. Microanisotropy imaging: quantification of microscopic diffusion anisotropy and orientational order parameter by diffusion MRI with magic-angle spinning of the q-vector. *Front Phys*. 2014;2(February). doi:10.3389/fphy.2014.00011
49. Kaden E, Kelm ND, Carson RP, Does MD, Alexander DC. Multi-compartment microscopic diffusion imaging. *Neuroimage*. 2016;139:346-359. doi:10.1016/j.neuroimage.2016.06.002
50. Rafael-Patino J, Romascano D, Ramirez-Manzanares A, Canales-Rodríguez EJ, Girard G, Thiran JP. Robust Monte-Carlo Simulations in Diffusion-MRI: Effect of the Substrate Complexity and Parameter Choice on the Reproducibility of Results. *Front Neuroinform*. 2020;14:457195. doi:10.3389/FNINF.2020.00008/BIBTEX
51. Villarreal-Haro JL, Gardier R, Canales-Rodríguez EJ, et al. CACTUS: a computational framework for generating realistic white matter microstructure substrates. *Front Neuroinform*. 2023;17:1208073. doi:10.3389/FNINF.2023.1208073/BIBTEX
52. Huang SY, Witzel T, Keil B, et al. Connectome 2.0: Developing the next-generation ultra-high gradient strength human MRI scanner for bridging studies of the micro-, meso- and macro-connectome. *Neuroimage*. 2021;243. doi:10.1016/J.NEUROIMAGE.2021.118530
53. Mueller L, Tax CMW, Jones DK. Unprecedented echo times for diffusion MRI using connectom gradients, spiral readouts and field monitoring. *MAGNETOM Flash*. Published online 2019. Accessed December 14, 2023. [https://cdn0.scrvt.com/39b415fb07de4d9656c7b516d8e2d907/1800000006277360/3a1f90ead087/siemens-healthineers-magnetom-flash-74-ismrm-unprecedented-echo-times\\_1800000006277360.pdf](https://cdn0.scrvt.com/39b415fb07de4d9656c7b516d8e2d907/1800000006277360/3a1f90ead087/siemens-healthineers-magnetom-flash-74-ismrm-unprecedented-echo-times_1800000006277360.pdf)
54. Tax CMW, Rudrapatna US, Mueller L, Jones DK. Characterizing diffusion of myelin water in the living human brain using ultra-strong gradients and spiral readout. In: *ISMRM 27th Annual Meeting & Exhibition, 11-16 May 2019, Montréal, QC, Canada. Abstract #1115*. 2019. Accessed July 19, 2024. <https://archive.ismrm.org/2019/1115.html>
55. Lee HH, Chan KS, Novikov DS, Fieremans E, Huang SY. Axon Diameter Mapping from Myelin Water Diffusion MRI. *IEEE Trans Med Imaging*. Published online 2026. doi:10.1109/TMI.2026.3664328
56. Lam SK, Pitrou A, Seibert S. Numba: A LLVM-based Python JIT Compiler. *Proc LLVM-HPC 2015 2nd Work LLVM Compil Infrastruct HPC - Held conjunction with SC 2015 Int Conf High Perform Comput Networking, Storage Anal*. 2015;2015-January. doi:10.1145/2833157.2833162

57. Sukstanskii AL, Yablonskiy DA. Effects of restricted diffusion on MR signal formation. *J Magn Reson*. 2002;157(1):92-105. doi:S1090780702925826 [pii]
58. Avram A V., Guidon A, Song AW. Myelin water weighted diffusion tensor imaging. *Neuroimage*. 2010;53(1):132-138. doi:10.1016/j.neuroimage.2010.06.019
59. Brusini L, Menegaz G, Nilsson M. Monte Carlo Simulations of Water Exchange Through Myelin Wraps: Implications for Diffusion MRI. *IEEE Trans Med Imaging*. 2019;38(6):1438-1445. doi:10.1109/TMI.2019.2894398
60. Andrews TJ, Osborne MT, Does MD. Diffusion of myelin water. *Magn Reson Med*. 2006;56(2):381-385. doi:10.1002/MRM.20945